

Particle-in-cell methods in edge plasma physics: the PICLS code

A. Bottino¹, A. Stier¹, M. Boesl², T. Hayward-Schneider¹,
A. Bergmann¹, D. Coster¹, S. Brunner³, G. Di Giannatale³ and
L. Villard³

¹Max-Planck-Institut für Plasmaphysik, 85748 Garching, Germany

²Spark e-Fuels GmbH, Berlin, Germany

³Swiss Plasma Center, École Polytechnique Fédérale de Lausanne, Switzerland

E-mail: alberto.bottino@ipp.mpg.de

August 2024

Abstract. Over the past decades, multiple gyrokinetic codes have shown to be able to simulate turbulence and associated transport in the core of Tokamak devices. However, their application to the edge and scrape-off layer (SOL) region presents significant challenges. To date, only few codes and models have been adapted to SOL/edge conditions. To further study the SOL region in particular, with its steep temperature and density gradients as well as large fluctuation amplitudes, the full-f particle-in-cell code PICLS has been developed. PICLS is based on a full-f gyrokinetic model with linearised field equations, considers kinetic electrons and uses logical sheath boundary conditions. In the past, PICLS was verified by applying it to a well-studied 1D parallel transport problem during an edge-localized mode in the SOL under both collisionless and collisional conditions, for which a Lenard-Bernstein collision operator was implemented. PICLS recently was extended towards three spatial dimensions to study turbulence in open-field-line regions in slab and closed-field-line toroidal geometries. In this work, we will focus on the models and methods we used for extending the code towards three spatial dimensions, including validation efforts and comparisons with other existing codes in closed-field-line geometry.

1. Introduction

Plasma theory and simulation of Tokamak plasmas advanced significantly during the past decades. In particular, gyrokinetic simulations have been proven to largely reproduce turbulence transport in the core, the innermost and hottest region of the plasma, where fusion power will be produced. The magnetic flux surfaces in the core region are nested and closed. The edge region is the subsequent region further towards the plasma wall, which also is characterized by closed flux surfaces. It is a rather thin layer and compared to the core often exhibits steep pressure gradients [1]. Once crossing the last closed flux surface (LCFS or Separatrix) an often even thinner layer of open field lines begins, the scrape-off layer (SOL). Here, the open field lines wind around

toroidally several times before they hit the divertor target. Thus, in the SOL particles are lost to the machine surface. In general, the greatest part of the plasma lies within the core and edge region. This is required, to achieve high enough confinement for the fusion reaction. Particles that would be confined by the closed flux surfaces, however, can be transported across the surfaces by turbulence and collisions. In the SOL, plasma that is transported out of the confined region, in general is lead to the divertor targets before it can reach the wall. This region is highly important for regulating the impurity level and confining the plasma. Plasma dynamics in the SOL are defined by a balance of plasma outflow from the core, turbulent transport across magnetic field lines, parallel flow and losses towards the divertor targets [2, 3, 4]. Typical characteristics for the SOL are low plasma density and temperature ($T_e \sim 10 - 100\text{eV}$, due to the plasma-wall interaction [1]), high collisionality and large-scale turbulence of amplitudes of order of unity compared to the background. Experimentally measured profiles confirmed these large amplitude fluctuations and the exponential decay of radial profiles. The complex physics in the SOL region also increases the complexity for plasma modeling and simulation [5]. For example, in the parallel direction along the field lines, electrons hit the divertor faster than ions, due to their higher mobility. The plasma establishes a thin layer of net positive charge of a few Debye lengths (due to Debye shielding), directly at the plasma-wall interface, the so-called Debye sheath [2]. This layer builds up a potential barrier that accelerates incident ions into the wall and repels incident electrons (only the fastest electrons can overcome the potential barrier). The particle fluxes of both species are kept approximately equal, thus the plasma is maintained quasi-neutral. The SOL plasma properties and the particle and energy flux towards the surface are significantly influenced by this sheath. In general plasma/wall boundary conditions are very challenging, due to the very fast dynamics of the plasma at the interface, combined with complicated geometries, requiring body-fitted unstructured meshes or remeshing strategies which can be time consuming. On the other hand, penalization techniques [6] have been proven to be an efficient tool to model efficiently the plasma/limiter interaction. Moreover, neutral gas dynamics also plays a major role in the SOL region, by decreasing the temperature and increasing the collisionality.

Apart from that, the size of plasma structures ranges from the gyroradius to machine size with strong gradients perpendicular and along the field lines. Also time scales vary in a wide range between the gyromotion and turbulence time scales. Fluctuations are of the order of unity compared to the background, which means that in simulations a *linearization* of quantities (i.e., splitting the distribution function in a constant background and a small perturbation $f = f_0 + \delta f$) as often applied in the plasma core is not valid anymore. And finally, also the divertor geometry adds up to the increase in complexity.

Although there exist fully six-dimensional kinetic code developments [7, 8], large time and length scale Tokamak simulations that solve the Vlasov–Maxwell or Vlasov–Poisson equations require processing and memory capabilities that are far beyond what nowadays supercomputers can provide. Even now, when we approach exascale computing, the

simulations are still way too costly. To cope with these computational restrictions, physical approximations are required to reduce the numerical calculation efforts.

Simulations within the SOL have been and are still primarily performed with the help of fluid- & gyrofluid-based codes, e.g. [9, 10, 11, 12, 13, 14]. The key advantage of fluid codes is their computationally relatively low effort, compared to kinetic approaches. Nevertheless, kinetic effects play an important role in edge plasmas with steep gradients and including the open-field region [15]. Therefore, there are major efforts to apply gyrokinetic first-principle codes to SOL and edge plasma. The underlying physical model is a 5D description of low-frequency plasma dynamics reduced from the initial 6D kinetic equations [16, 17, 18]. In the plasma core gyrokinetic simulations are nowadays widely used and produce comparable turbulence results across various codes. But due to the extremely rich physics in the plasma edge/SOL, only few codes have been adapted to simulate the plasma periphery. To only name a few challenges that are especially relevant for gyrokinetic models in this region: large amplitude fluctuations, sheath boundaries, wide range of space and time scales, atomic physics, etc. As a result, code developments in the SOL need to specifically address these complications. Currently, one of the most advanced gyrokinetic code is probably XGC, which gained popularity with its calculation of the ITER scrape-off layer width [19] and it was recently applied to model tungsten transport in the pedestal and turbulence transport in the presence of resonant magnetic perturbations (see Refs. [20, 21, 22] and references therein).

Most commonly, there are two basic methods applied to numerically solve the gyrokinetic system, particle-in-cell (PIC) methods (e.g. [23, 24, 25]) and continuum methods (e.g. [26, 27]). In the continuum case (also called “Eulerian”), the 5D gyrokinetic equations are discretized on a fixed phase-space mesh and solved on this mesh. The resulting partial differential equations are then solved with numerical methods like finite-volumes, finite-elements, etc. Equal to the PIC approach, in continuum codes the 3D fields are calculated by using grid-based algorithms. In a PIC code Monte Carlo methods are applied that approximate integrals over phase space (moments of the particle distribution function) by a finite number of markers [28]. In a more tangible picture, the markers can be described as “superparticles” that comprise many physical particles. The number of markers used in practice is much lower than the physical particle number [29]. In a very simplified picture, the PIC algorithm applied on gyrokinetic plasma simulations advances these particles according to the Euler Lagrange equations, with the help of a force field which is set up by a charge/current distribution ([30],[31]). More specifically, markers are initially distributed in the phase space and according to their positions, the 3D field equations are solved from this charge distribution on a fixed grid. Then the resulting fields are interpolated back to the marker positions and using these fields the markers are advanced to their new position according to the gyrokinetic Euler-Lagrange equations. This procedure is then repeated again and again for the new distributions. One of the main challenges of PIC algorithms is their inherent statistical noise in the distribution function, due to their Monte Carlo sampling approach. For N markers, this error scales with $1/\sqrt{N}$. This effect is extremely relevant for the

validity of results and thus several techniques for noise reduction have been developed, e.g. [32, 33, 34]. Another often discussed problem resulting from statistical noise is the so-called Ampère’s law cancellation problem in electromagnetic simulations, where two large terms in the Ampère’s law cancel out numerically at average to high plasma β and small perpendicular wave numbers. But since its discovery, various mitigation techniques were introduced with convincing results [35, 36, 37, 38] and nowadays it is not seen as a showstopper anymore.

Numerical models and challenges behind PIC and continuum codes for edge/SOL applications are quite different (see e.g. [39, 40, 41, 42, 43, 44, 45, 46]). Thus, to be able to perform reliable quantitative studies, it is important to develop both further and use cross-checks between both methods for validation. In this paper we present the gyrokinetic full-f particle-in-cell code for open field lines in the SOL, called PICLS. PICLS is a gyrokinetic Particle-in-Cell code for simulations in the scrape-off layer, or open field line regions. The code was initially designed to study sheath boundary models and heat and particle fluxes from the plasma towards the wall, but gets constantly extended towards more complicated open field line geometries. The PICLS code was already introduced in [47, 48], but limited to the a single spatial dimension (1D). While a 1D code can be used to model the parallel transport in open field lines, the study of the cross-field transport in the SOL requires a 3D model. For magnetic fusion devices, such as tokamaks, in the SOL the propagation of blobs (also called plasma filaments) can convectively transport heat, particles, momentum and current across magnetic field lines and thus lead to a highly discontinuous cross-field transport (see e.g. [1]). It is believed that in tokamak devices across the blob cross-section the curvature and $\nabla\mathbf{B}$ forces establish a charge-separated dipole potential. This mainly causes an outward radial propagation of the blob, due to convective $\mathbf{E} \times \mathbf{B}$ transport. For advanced fusion devices, such as ITER and beyond, the balance between parallel and cross-field transport in the SOL is decisive for how heat and particles are exhausted ([49]). Thus, for future performance predictions of fusion devices, modeling of these turbulent transport phenomena in the SOL region is important. Therefore, we had to extend our previous 1D code to a 3D version which can cope with different geometries and includes magnetic curvature and $\nabla\mathbf{B}$ terms. In this work, the 3D version of the PICLS code is presented, together with some validation efforts and comparisons with existing codes.

Just as a short side note, this is also the reason for its name “PICLS”, a combination of “PIC” for Particle-In-Cell and “LS” for Logical Sheath [50]. So far, a rather simple 1D (one spatial domain) case and a more advanced 3D case are implemented in PICLS.

2. The PICLS code

2.1. The physical model

In general, the physical model behind PICLS is derived from a gyrokinetic Lagrangian (see e.g. [17]), using the Hamiltonian for the particle species p

$$H_p = m_p \frac{v_{\parallel}^2}{2} + \mu B + e_p J_{p,0} \phi - \frac{m_p c^2}{2B^2} |\nabla_{\perp} \phi|^2, \quad (1)$$

with the velocity variables v_{\parallel} (parallel velocity), $\mu = m_p v_{\perp}^2 / (2B)$ (magnetic moment), the magnetic field strength B , the mass m_p and charge e_p ; c is the speed of light. The gyroaveraging operator is indicated as $J_{p,0}$. In the following, variables with a perpendicular subscript lie within the plane perpendicular to the magnetic background field \mathbf{B} , whereas variables with a parallel subscript lie along the magnetic background field. Details about the specific derivation of the PICLS model can be found in [51].

The corresponding Euler-Lagrange equations are

$$\begin{aligned} \dot{\mathbf{R}} &= v_{\parallel} \frac{\mathbf{B}^*}{B_{\parallel}^*} + \frac{c}{e_p B B_{\parallel}^*} \mathbf{B} \times \\ &\quad \left[\mu \nabla B + e_p \nabla J_{p,0} \phi - \frac{m_p c^2}{2B^2} \nabla |\nabla_{\perp} \phi|^2 + \frac{m_p c^2}{B^3} \nabla B |\nabla_{\perp} \phi|^2 \right], \\ \dot{v}_{\parallel} &= -\frac{\mathbf{B}^*}{B_{\parallel}^*} \frac{1}{m_p} \cdot \left[\mu \nabla B + e_p \nabla J_{p,0} \phi - \frac{m_p c^2}{2B^2} \nabla |\nabla_{\perp} \phi|^2 + \frac{m_p c^2}{B^3} \nabla B |\nabla_{\perp} \phi|^2 \right], \\ \dot{\mu} &= 0. \end{aligned} \quad (2)$$

The Vlasov equation is

$$\frac{d}{dt} f = \frac{\partial f}{\partial t} + \dot{\mathbf{R}} \cdot \nabla f + \dot{v}_{\parallel} \frac{\partial f}{\partial v_{\parallel}} = C, \quad (3)$$

where C indicates a generic collision operator and upper dot correspond to Lagrangian derivatives. The polarization (Poisson) equation, in the long wavelength limit, has the form of a nonlinear elliptic equation

$$-\sum_p \nabla_{\perp} \frac{n_i m_p c^2}{B^2} \nabla_{\perp} \phi = \sum_p \int dW e_p J_{p,0} f. \quad (4)$$

However, in this work we considered a simpler model, for which the so-called linearized polarization approximation has been used (see [23] end references therein). Nevertheless, ion finite-Larmor radius effects (FLR) are retained in both the polarization density and in the gyroaverage operator. The full derivation of the model equations can be found in [47]. In this simpler case, the Euler-Lagrange equations do not contain second order terms

$$\begin{aligned} \dot{\mathbf{R}} &= v_{\parallel} \frac{\mathbf{B}^*}{B_{\parallel}^*} + \frac{c}{e_p B B_{\parallel}^*} \mathbf{B} \times [\mu \nabla B + e_p \nabla J_{p,0} \phi], \\ \dot{v}_{\parallel} &= -\frac{\mathbf{B}^*}{B_{\parallel}^*} \frac{1}{m_p} \cdot [\mu \nabla B + e_p \nabla J_{p,0} \phi], \\ \dot{\mu} &= 0. \end{aligned} \quad (5)$$

The polarization equation is now a linear elliptic equation because the gyrocenter density $n_{\mathbf{i}}$ is replaced by the equilibrium background density $n_{\mathbf{i},0}$

$$-\sum_p \nabla_{\perp} \frac{n_{\mathbf{i},0} m_p c^2}{B^2} \nabla_{\perp} \phi = \sum_p \int dW e_p J_{p,0} f. \quad (6)$$

In addition to this, collisions, while being included in PICLS, are not considered in this work. The Vlasov equation becomes

$$\frac{d}{dt} f = \frac{\partial f}{\partial t} + \dot{\mathbf{R}} \cdot \nabla f + v_{\parallel} \frac{\partial f}{\partial v_{\parallel}} = 0. \quad (7)$$

The total conserved energy in the electrostatic model is [52, 51]

$$\mathcal{E}_{\text{tot}} = \sum_p \int dW dV H_p f_p \quad (8)$$

$$= \mathcal{E}_{\text{k}} + \mathcal{E}_{\text{f}} = \sum_p \int dW dV H_{p,0} f_p + \sum_p \frac{1}{2} \int dW dV e_p J_{p,0} \phi f_p, \quad (9)$$

with $H_{p,0} = \frac{1}{2} m_p v_{\parallel}^2 + \mu B$ in the kinetic part.

2.2. Normalization

In PICLS we implemented two different sets of normalization schemes. In the first set, mostly used for debugging, the code uses the standard CGS units of the physical quantities. In the second one, all the equations are normalized using input reference values before numerical solutions are calculated. Given a dimensional quantity x , we split it into a dimensional constant \bar{x} and a dimensionless quantity \tilde{x} , as illustrated in Table 1.

Only five of the dimensional quantities of Table 1 are independent. In PICLS, the independent normalization quantities are chosen to be, and their normalization is described in Table 2.

Where N_{phys} is the total number of physical electrons, V is the plasma volume and r_{ref} an arbitrary chosen radial reference point. The PICLS output is always in CGS units.

2.3. Discretization

The most important difference between the 1D and 3D version of PICLS is the introduction of the gyroaverage operator. As in the ORB5 code, the gyroaverage is performed in real space with a discrete average on the gyroring of each single marker. The standard PIC cycle, based on particle pushing and charge deposition is therefore modified by setting up ‘‘Larmor points’’ on the Larmor radius around the gyrocenter before the charge deposition and by averaging across these Larmor points directly after the field calculation, following Ref. [53]. The PICLS computational cycle is summarized

Table 1. PICLS geometric setup and initial perturbation for the four simulations of Fig. 6. Each of the four simulations is characterized by different values of q . The poloidal and toroidal mode numbers are selected such that $k_{\parallel} = 1$ in all cases. Consequently, in each simulations the value of m has been adapted to the corresponding q : $m = 5$ for $q = 5/3$, $m = 10$ for $q = 10/3$, $m = 15$ for $q = 15/3$ and $m = 20$ for $q = 20/3$.

Quantity	Label 2	Normalisation
time	t	\tilde{t}
length	l	\tilde{l}
mass	m	$\tilde{m}\bar{m}$
charge	q	$\tilde{q}\bar{q}$
Magnetic field	B	$\tilde{B}\bar{B}$
Temperature	T	$\tilde{T}\bar{T}$
velocity	v	$\tilde{v}\bar{v}$
magnetic moment	μ	$\tilde{\mu}\bar{\mu}$
electrostatic pot.	ϕ	$\tilde{\phi}\bar{\phi}$
electromagnetic pot.	A_{\parallel}	$\tilde{A}_{\parallel}\bar{A}_{\parallel}$
current density	j_{\parallel}	$\tilde{j}_{\parallel}\bar{j}_{\parallel}$
charge density	ρ	$\tilde{\rho}\bar{\rho}$

Table 2. Normalization quantities in PICLS.

Parameter	Normalisation	Description
\bar{B}	B_0	magnetic field strength
\bar{m}	input or m_e	mass
\bar{q}	input or $ q_e $	charge
\bar{T}	T_e at r_{ref}	temperature
\bar{n}	N_{phys}/V	density

in Fig. 1. The number of Larmor points used to calculate the average depends on the thermal velocity of the particles and thus on the size of the gyroradius [54, 55]. A larger gyroradius requires a higher number of Larmor points, since the points are distributed further and thus the probability for the fields to significantly vary their value along the gyroring, significantly increases.

These procedures are repeated again and again in so-called timesteps via a Runge-Kutta 4th order time integrator and for each time step system diagnostics can be extracted. Note that PICLS also allows for a drift-kinetic model for ions and electrons. In this case, the only FLR effect retained is the polarization density, while all the gyroaveraged quantities are replaced by their value at the gyro-center position, details can be found in [23]. In all the simulations presented in this paper, a drift-kinetic model is used for the electrons and the electron polarization density is neglected in the Poisson equation.

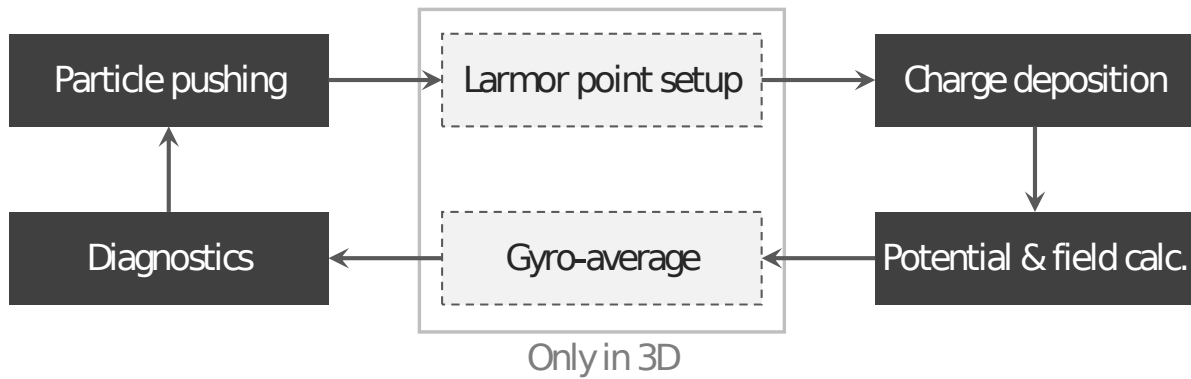


Figure 1. Schematic representation of main procedures applied at each time step of simulation. Procedures with bright gray background are only applied in 3D case if Larmor radius effects are considered. Other procedures are used for each dimensionality (1D and 3D).

2.4. Initialization of the markers

An important difference between PICLS and other existing PIC codes like ORB5 is that here the entire gyrocenter distribution function $f(\mathbf{R})$ is represented by discrete markers. In the full-f representation, where the whole distribution will be simulated, the particle distribution function thus can be expressed as

$$f(\mathbf{R}, v_{\parallel}, \mu, t) = \sum_{n=1}^N w_n(t) \delta(\mathbf{R} - \mathbf{R}_n(t)) \delta(v_{\parallel} - v_{\parallel n}(t)) \delta(\mu - \mu_n), \quad (10)$$

with N the number of markers, w_n the marker weights, \mathbf{R}_n their position, $v_{\parallel n}$ their parallel velocity and μ_n their (constant) magnetic moment. With the definition for the initial number of physical particles, $N_{\text{phys}} = \int n_0(\mathbf{R}) d\mathbf{R}$, the weights in our case are uniformly initialized with

$$w_n = \frac{1}{N}, \quad (11)$$

for all markers. The weights for the full-f case are constant and thus do not change over time:

$$\frac{d}{dt} w_n = 0. \quad (12)$$

More details about the exact definition of the marker weights for PICLS and ORB5 can be found in Ref. [56]. In the 3D version of PICLS, markers are loaded in phase-space using importance sampling. In all the simulations presented in this work, a Maxwellian loading has been used, proportional to the physical equilibrium distribution function, chosen to be a Maxwellian described by density and temperature profiles, function of the radius only. As a result, the marker weights are all the same and normalized in a way that their sum corresponds to one. An example of Maxwellian loading is illustrated in the histograms of Fig. 2, where the particle distribution in velocity has been reconstructed after the initial loading, by binning a set of test particles (6M) in radius and $|v|$.

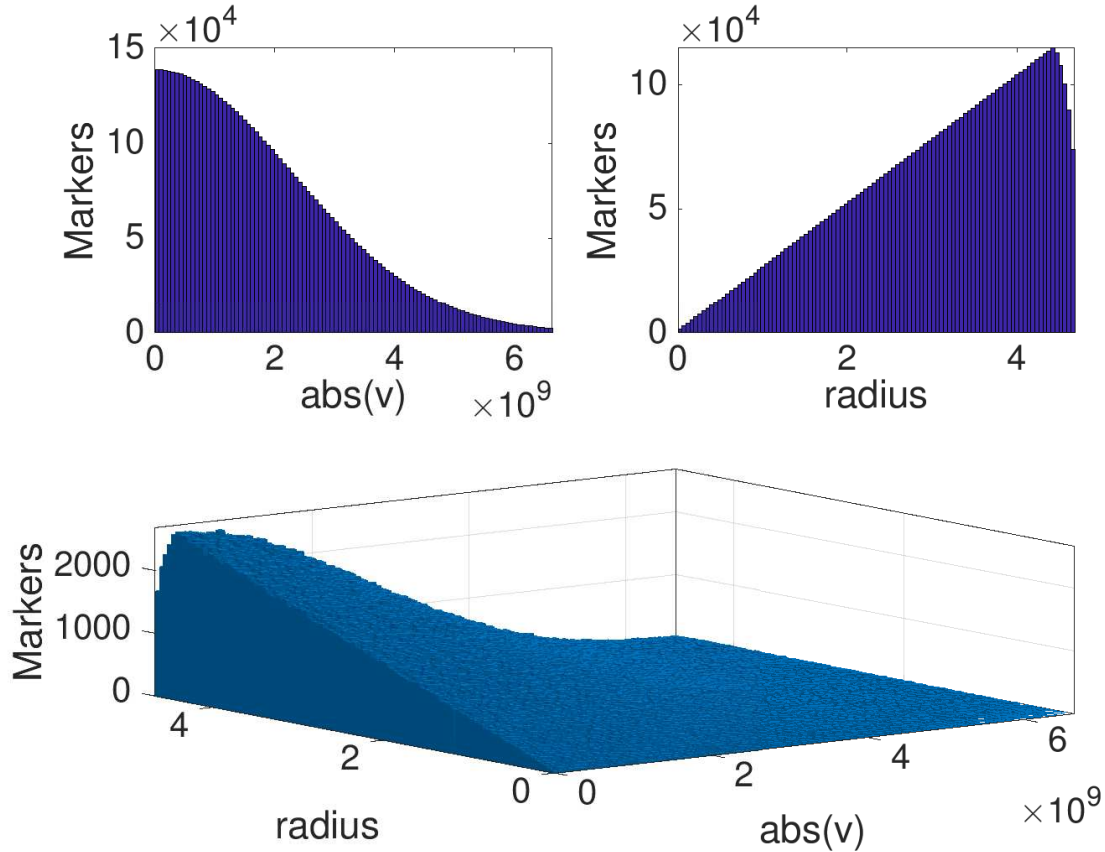


Figure 2. Example of Maxwellian loading. Histograms in velocity and radius for a subset of 6 million test particles, loaded assuming a Maxwellian probability distribution function with constant T and n profiles. The analytically prescribed Maxwellian function is correctly reproduced by the markers.

2.5. 3D finite element solver

PICLS uses a Finite Element (FE) discretization scheme with B-splines as basis functions. Solving the 3D electric potential with finite elements in all three dimensions can be computationally extremely costly, depending on the number of grid cells in each direction (n_x, n_y, n_z) or (n_r, n_θ, n_φ). However, if the regarded problem is periodic in one of the three dimensions, a Discrete Fourier Transform (DFT) can be applied to the B-spline coefficients in the periodic dimension. Depending on the size of the problem, this can reduce the computational cost of the simulation significantly. The remaining two dimensions can still be calculated based on a 2D finite element field solver. This Fourier enhanced finite element solver of PICLS has been described in detail in a dedicated paper [57]. Assuming φ being the periodic direction, the result is that the large matrix corresponding to the 3D Poisson equation is replaced by a set of n_φ smaller matrices

equations (2D), making the solver straightforwardly parallelizable,

$$\sum_{j'k'} \phi_{j'k'}^{(n)} A_{j'k'jk} = \frac{b_{jk}^{(n)}}{M^{(n)}}, \quad (13)$$

with

$$A_{j'k'jk} = \int N(s, \theta) \nabla_{\perp}(\Lambda_{j'}(s) \Lambda_{k'}(\theta)) \nabla_{\perp}(\Lambda_j(s) \Lambda_k(\theta)) J(s, \theta) ds d\theta \quad (14)$$

and

$$\sum_{j'k'} \phi_{j'k'}^{(n)} \int N(s, \theta) \nabla_{\perp}(\Lambda_{j'}(s) \Lambda_{k'}(\theta)) \nabla_{\perp}(\Lambda_j(s) \Lambda_k(\theta)) J(s, \theta) ds d\theta = \frac{b_{jk}^{(n)}}{M^{(n)}}, \quad (15)$$

with:

$$N(s, \theta) = \sum_{s=i} \frac{q_s^2 n_s}{T_s} \rho_s^2. \quad (16)$$

Note that this procedure relies on the polarization density factor $N(s, \theta)$ not depending on φ . Practically, after the usual charge assignment, a DFT is applied on the spline coefficients in φ to get the Fourier components $b_{jk}^{(n)}$. Each $b_{jk}^{(n)}$ is then divided by the analytically known term $M^{(n)}$, which corresponds to the mass matrix of the B-spline basis in toroidal-Fourier space (see Ref. [57] for the full derivation). The resulting matrix problem is solved using a direct solver (LAPACK [58]). Once the $\phi_{j'k'}^{(n)}$ Fourier coefficients are known, the electrostatic potential can be reconstructed in any point in the domain.

Here we present a convergence order analysis of the Poisson solver using the Method of Manufactured Solutions (MMS) [59]. With this method, a manufactured solution is provided to the solver by adding proper source terms to the discrete equation. The deviation of the numerical solution of the equation compared to the provided manufactured solution is then checked.

In our specific case, we use the method of manufactured solution for the Poisson equation. The Poisson equation of PICLS has the form

$$N(f)[\phi_1] = S_{\phi_1} \quad (17)$$

where $N(f)$ is a generic integro-partial differential operator.

We perform the following procedure:

- (i) First a specific source S_{ϕ_1} is constructed, for which a given function, ϕ_{1MMS} is an exact solution of the system. The source ϕ_1 is calculated by plugging the solution ϕ_{1MMS} into equation 17. The function ϕ_{1MMS} is called the manufactured solution.
- (ii) The normal solver routine is applied to get the solved potential ϕ_1 .
- (iii) The constructed potential is then compared with the solved one to study the similarity of both and thus identify potential deviations. It is possible to calculate relative errors of the numerical solution and to verify the order of convergence of the numerical scheme.

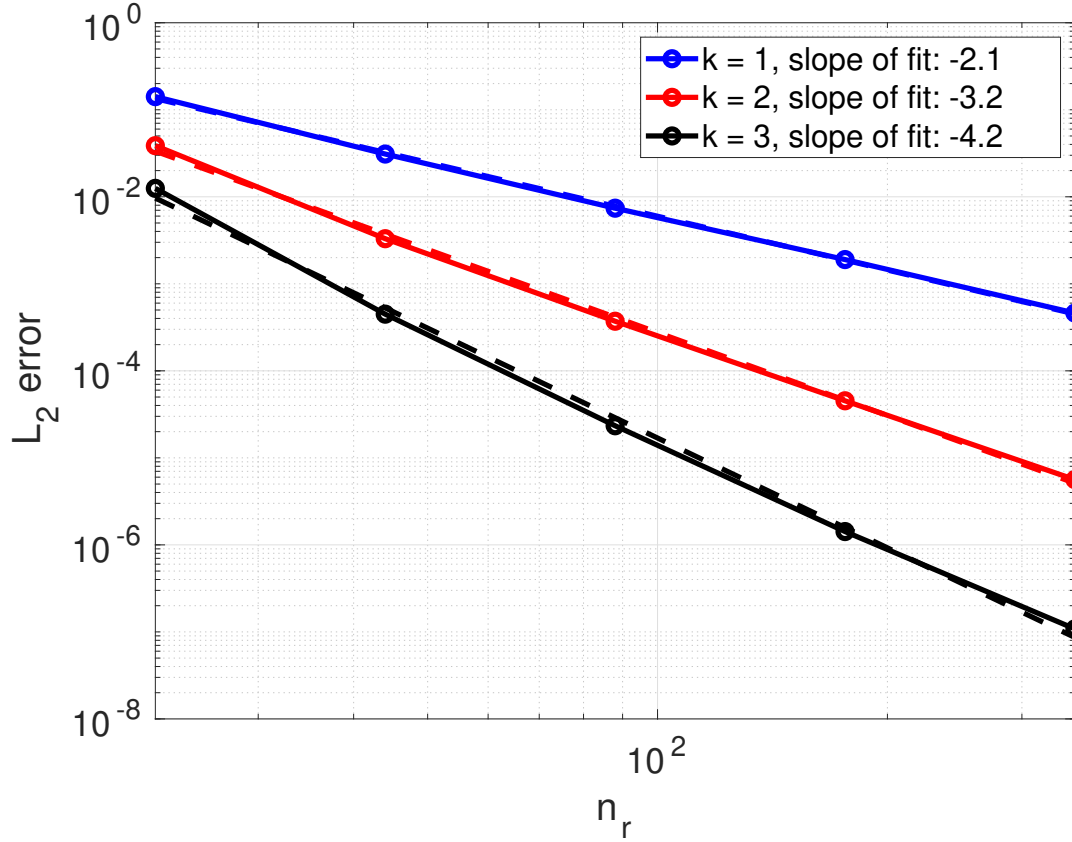


Figure 3. Verification of the converge of the Poisson solver using the L_2 error. The initial resolution is ($n_r = 22, n_\theta = 32, n_\varphi = 8$). Although the value of n_r is used as label for the x-axis, the resolution in all directions was re-scaled by the same factor as n_r . Final resolution ($n_r = 352, n_\theta = 512, n_\varphi = 128$)

The chosen manufactured solution is

$$\phi_{1MMS} = \tilde{a}(g(r) + \alpha r + \beta) \sin(m_i \theta) \sin(n_i \varphi), \quad (18)$$

with

$$g(r) \equiv \exp\left(-\frac{1}{2} \left(\frac{r - r_0}{\sigma_r}\right)^2\right). \quad (19)$$

Where \tilde{a} , m_i , n_i , r_0 and σ_r are input parameters and α and β are constants which are determined by the boundary conditions in r . Dirichlet boundary conditions are used, which imply $\beta = -g(r = 0)$ and $\alpha = 0$. Assuming a flat density profile, and choosing $n_i = 1$ and $m_s = 1$, the corresponding source is:

$$S_{\phi_1} = -\frac{1}{r} \frac{1}{B^2} \frac{\partial \phi_{1MMS}}{\partial r} + \frac{2}{B^3} \frac{\partial B}{\partial r} \frac{\partial \phi_{1MMS}}{\partial r} - \frac{1}{B^2} \frac{\partial^2 \phi_{1MMS}}{\partial r^2} - \frac{1}{B^2 r^2} \frac{\partial^2 \phi_{1MMS}}{\partial \theta^2} \quad (20)$$

In the following tests we used $m_i = 5$, $n_i = 2$, $q = 2$, $r_0 = 3.02\text{cm}$ and $\sigma_r = 0.6\text{cm}$. The screw-pinch geometry has the following parameters: $R = 774\text{cm}$, $B_0 = 1\text{T}$ and $a = 6.05\text{cm}$. The simulation box ranges from $r = 0$ to $r = 6.05\text{cm}$. As mentioned

before, the density profile is flat. The initial resolution is determined by the number of splines in the three directions, set to $(n_r = 22, n_\theta = 16, n_\phi = 8)$. The convergence of the algorithm is tested by doubling the resolution in each direction. Given a discrete vector field $\phi_p = \phi(r_i, \theta_j, \phi_k)$ with $i = [1 : \bar{n}_r]$, $j = [1 : \bar{n}_\theta]$ and $k = [1 : \bar{n}_\phi]$, we define an error, L_2 , using the L_2 norm

$$\|\phi\|_{L_2} = \sqrt{\sum_p \phi_p^2}, \quad (21)$$

with

$$L_2 = \frac{\|\phi - \phi_{MMS}\|_{L_2}}{\|\phi_{MMS}\|_{L_2}} \quad (22)$$

Results are shown in Fig. 3 for linear ($k = 1$), quadratic ($k = 2$) and cubic ($k = 3$) splines. While only n_r is reported as a label for the x-axis, actually the number of splines in all directions has been re-scaled, ranging from $(n_r = 22, n_\theta = 32, n_\phi = 8)$ to $(n_r = 352, n_\theta = 512, n_\phi = 128)$. The slope of the linear fit on the log-log plot is reported in the legend of the two figures. The slope of the error curve is mathematically expected to be equal to $k + 1$ which matches the results shown here in good approximation. In those tests the number of grid points used for comparing the two solutions are $\bar{n}_r = 90$, $\bar{n}_\theta = 100$ and $\bar{n}_\phi = 110$.

2.6. Geometries

In PICLS the markers are loaded in a Cartesian space of dimension (L_x, L_y, L_z) . The particle motion in the absence of fluctuations is determined by the background magnetic field. Note that an external electrostatic potential can also be imposed on the particle equations of motion. Moreover, two different elliptic solver are implemented in PICLS. The first one is in Cartesian coordinates, where the y coordinate is periodic while (zero or nonzero) Dirichlet boundary conditions can be applied in x and z . The second one is similar to the ORB5 solver, based on polar coordinates, in which only one coordinate (radius) is non periodic. The main difference between the two solver types is that in the polar case the FT-direction lies along the main B-field direction while in the Cartesian solver it is directed perpendicularly to the B-field. At the moment, three different magnetic geometries are implemented in PICLS (see also Fig. 4 for illustration):

- (i) **Cylinder:** In this case, the geometry is cylindrical with the coordinates (s, θ, z) , where s is the radius r of the cylinder normalized to the minor radius a , θ the poloidal angle and z goes in the ‘‘toroidal’’ direction. The cylinder geometry can also be used as cylindrical Tokamak, for which z is replaced by the toroidal angle φ . In this case, the magnetic field B has only a component in z direction and also the Fourier transformed direction is along z . In this case, only one direction, s , can be non periodic.
- (ii) **Pinch:** This geometry in general is similar to the ‘‘Cylinder’’ case, except that the B-field can have an additional component in the poloidal θ direction.

- (iii) **Slab**: Here, we use a 3D slab geometry, with the spatial coordinates (x, y, z) . The magnetic field is aligned along the z coordinate, but different from the “Cylinder” and “Pinch” case, the Fourier transformed direction is along the perpendicular y direction. Both x and z direction are non periodic and on z (logical) sheath boundary conditions can be applied. The logical sheath model used PICLS is based on the Parker’s model ([60]). The implementation of this model in PICLS can be found, for the 1D case, in [47]. In the 3D code, the total parallel current to the wall is set to zero ($j_{\parallel} = 0$) at every point in time and thus the wall can be regarded as insulating. From a physical point of view, incident ions that flow towards the sheath boundary are accelerated by the dropping sheath potential. Whereas electrons are only absorbed if their velocity is high enough to overcome the sheath potential drop at the wall. Electrons below this critical velocity are reflected back into the domain. Details and validation efforts for the 3D PICLS sheath model will be published elsewhere. In the future, more sophisticated sheath models could be considered (see, e.g. [61]).

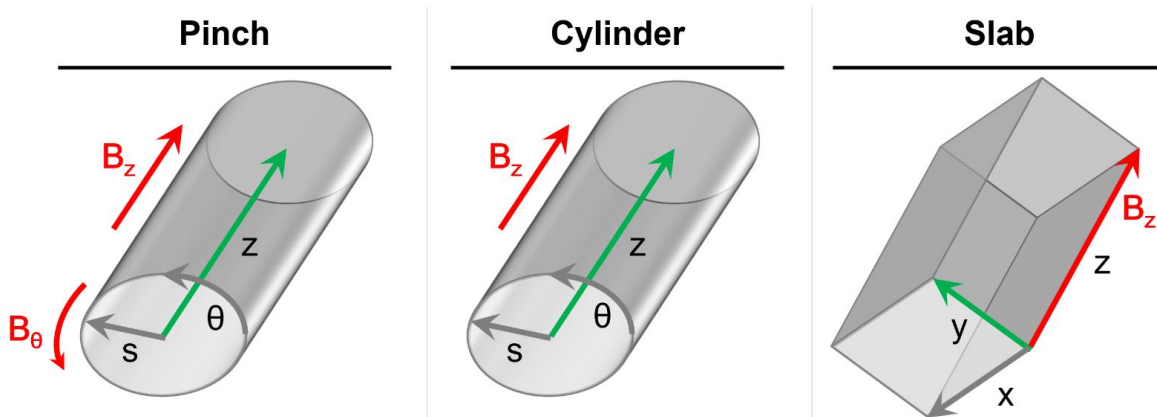


Figure 4. Illustration of the three different geometries “Pinch”, “Cylinder”, and “Slab” that are currently implemented in PICLS. “Pinch” and “Cylinder” are implemented in cylindrical coordinates (s, θ, z) , whereas “Slab” uses (x, y, z) coordinates. The red arrows indicate the direction of the B-field of the respective geometry. The green arrows indicate the direction of the coordinate for the DFT of the electric field solver.

2.7. Parallelization

Running high resolution plasma simulations with a gyrokinetic full-f PIC code, in general means that a significant number of markers and grid cells is required. However, the more markers and cells we introduce, the higher the computational costs become. As a result, an efficient parallelization scheme needs to be implemented, to share data between multiple processors to join their computation resources and to optimize the memory use.

In PICLS, we use a hybrid OpenMP and MPI approach. The specific methods we apply

for the parallelization of the MPI tasks are called domain decomposition and domain cloning.

In the domain decomposition approach, the grid cells are split up into different domains. Each domain is then attributed to a MPI task and also the particles that are present within the cell at the specific time-step are attributed to this task. For our domain decomposition, we split the cells along the periodic Fourier transformed direction.

In the domain cloning [62] approach, however, the number of particles is divided between the number of defined MPI clones. Each clone has a copy of the whole domain field data to deposit the charges. The sums of the charges of each clone are then added up via MPI communication to calculate the source term for field equation. The fields are then solved and broadcast to all clones.

Each MPI task eventually is responsible for a specific clone and a specific domain. Within each of these MPI tasks, the particle operations are performed in parallel and OpenMP is applied, to optimally use computational resources. Since the particles can move from one domain to the other, according to their characteristic equations, a function "particle_move" is implemented that moves the particles from the exiting to the entering MPI domain for the calculations. In figure 5 this parallelization scheme is sketched.

Preliminary performance results on the MARCONI FUSION HPC system at CINECA

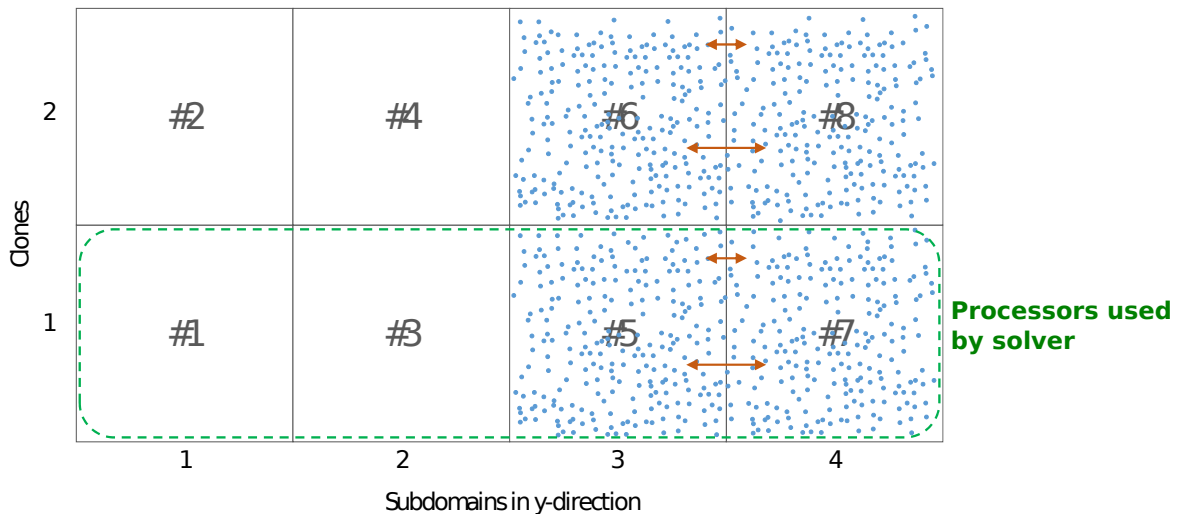


Figure 5. Illustration of the PICLS parallelization scheme with 4 domains and two clones. The blue dots represent the particles and the orange arrows the communication between the MPI domains. In the example, the communication is displayed exemplary for domains 3 & 4 and clones 1 & 2. With the green box we indicated to which processors the particle sums are reduced for the field solve. The total number of processors (indicated by #) is equal to the number of domains times the number of clones.

showed a speedup of 2.8 for realistic ITG turbulence simulations (see next Section) when moving from 20 nodes (960 cores) to 80 nodes (3840 cores) using 128 million markers.

Moreover, the weak scaling on number of marker is practically perfect when moving from 20 to 80 nodes.

Apart from general code optimization, additional effort will be needed to port the code to GPUs to fully exploit the capabilities of new computing systems. Potential options here are OpenACC and OpenMP-offload, which have to be further evaluated.

3. Verification

In this section we present some verification efforts for closed-field-line configurations, including a comparison with two production codes: the grid based GENE-X [46] code and the PIC code ORB5 [53]. All the simulations discussed in this section were performed using cubic B-splines ($k = 3$).

3.1. ITG modes, comparison with GENE-X

Going from a 1D to a 3D spatial domain is not trivial and requires careful implementation and testing. Several main aspects of our PIC algorithm, especially the field solver and the particle pusher, needed to be adjusted to allow for higher dimensional simulations. Therefore, the new code has been verified on the known problem of ITG (Ion Temperature Gradient) instabilities in a screw-pinch geometry, for which pre-existing results exist [46].

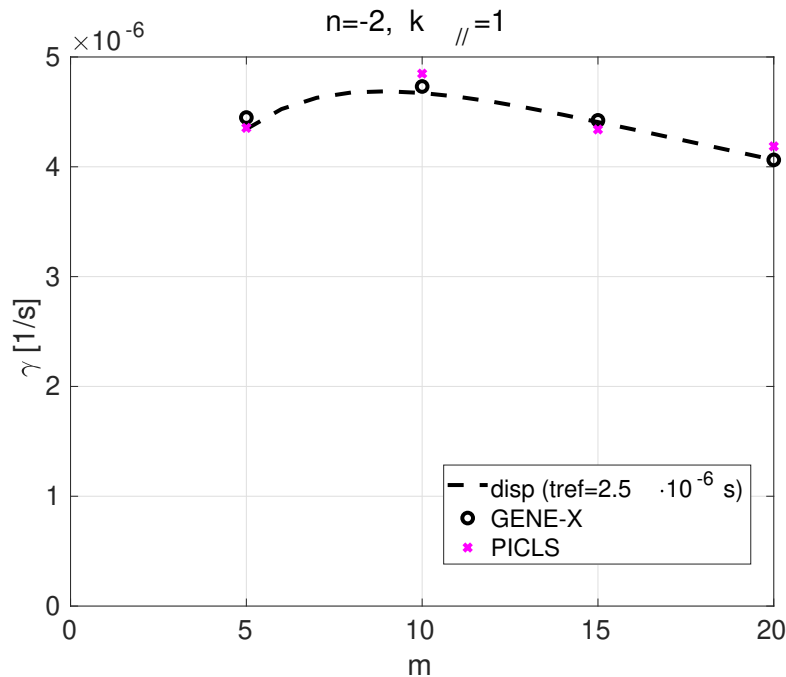


Figure 6. Growth rates measured via linear fits on a logarithmic plot of the L_2 norm of the potential, for different poloidal mode numbers, for a fixed $n = -2$ and for q -values adjusted to keep $k_{\parallel} = 1$ constant. PICLS results are in good agreement with both GENE-X and dispersion relation data.

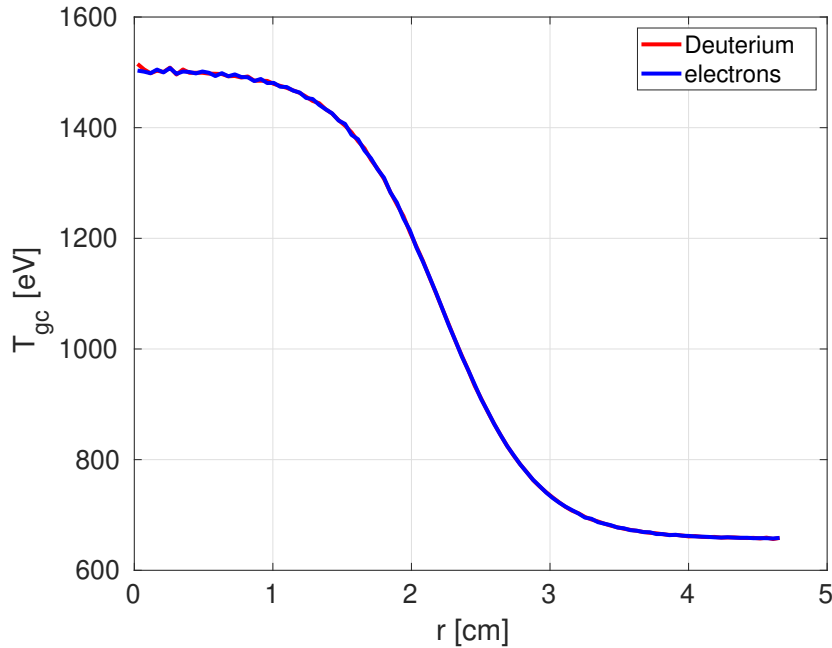


Figure 7. Temperature profiles calculated as moment of the marker distribution function, showing that the newly implemented Maxwellian loading routine provides the expected behavior in velocity space

The screw-pinch configuration (a.k.a. *straight Tokamak*) is a periodic system, based on a cylindrical pinch device with the coordinates (r, θ, z) , where r is the radius, θ the poloidal angle and z the coordinate along the cylindrical axis (or toroidal direction). Its name comes from the helical shape of the magnetic field with components in the z and θ direction. The electric potential solver we use for the screw-pinch is the solver in polar coordinates, with an DFT in the periodic toroidal z -direction, periodic boundary conditions in the poloidal direction and Dirichlet boundary conditions in the radial direction. The particles leaving the domain in the radial direction are destroyed and recreated randomly into the physical domain in order to keep the total number of physical particles fixed. The screw-pinch magnetic field in polar coordinates is

$$\mathbf{B} = B_0 \left(-\frac{r}{Rq_S(r)} \boldsymbol{\theta} + \mathbf{z} \right), \quad (23)$$

with the radius r , the q -factor $q_S(r) = q_0 + q_1 s^2$, the normalized radius $s = r/a$, the constant magnetic field B_0 and $R = L_z/2\pi$ (L_z is the length of the cylinder in z -direction). For a screw-pinch, Maxwellians are an exact equilibrium solution of the gyrokinetic system of equations. Therefore, in order to destabilize ITG modes an initial perturbation with a Gaussian radial shape and a fixed toroidal and poloidal number component is added to the ion density. Moreover, according to the dispersion relation, the Eigenvalues of a slab ITG mode are functions of the poloidal mode number m and the parallel wave number k_{\parallel} .

The simulation setup is described in [46] and summarized in Table 3.

Table 3. PICLS geometric setup and initial perturbation for the four simulations of Fig. 6. Each of the four simulations is characterized by different values of q . The poloidal and toroidal mode numbers are selected such that $k_{\parallel} = 1$ in all cases. Consequently, in each simulations the value of m has been adapted to the corresponding q : $m = 5$ for $q = 5/3$, $m = 10$ for $q = 10/3$, $m = 15$ for $q = 15/3$ and $m = 20$ for $q = 20/3$.

Parameter	Value	Description
a	4.68 [cm]	minor radius
R	77.0 [cm]	major radius
n_0	$0.5 \cdot 10^{13}$ [cm $^{-3}$]	density flat
$T_{e0} = T_{i0}$	1000 [eV]	Temperature at $s = 0.5$
m_e	$1 m_{elec}$	electron mass
m_i	$3972 m_{elec}$	ion mass (D)
ρ_s	0.32 [cm]	sound Larmor radius
k_{\parallel}	1	parallel wave number (fixed)
n	-2	toroidal mode number
q	5/3, 10/3, 15/3, 20/3	safety factors
m	5, 10, 15, 20	poloidal mode numbers

Note that in all those simulations a single n mode, $n = -2$ has been included in the simulation. The background temperature has been defined following the prescription provided in [46]. The results, summarized in Fig. 6, show an excellent agreement with the GENE-X results (from [46]) and the dispersion relation.

In PICLS, the growth rate has been calculated by taking a linear fit on the logarithmic plot of the L_2 norm of the electrostatic potential, during the linear phase of the simulation. Fig. 7 shows the ion and electron temperature profiles reconstructed by taking moments of the marker distribution function. This shows that the newly introduced importance sampling routines provide the expected Maxwellian loading in velocity space.

3.2. ITG turbulence

Using the same numerical setup of the GENE-X benchmark, described in the previous section, a set of turbulence simulations has been performed by increasing the number of toroidal mode numbers allowed in the simulation. Fig. 8 shows an example of such a simulation in which six toroidal mode numbers, $n = [0 : 5]$ are retained, for the $q = 10/3$ case. The initial perturbation has been kept the same as in the $k_{\parallel} = 1$ and $n = -2$ case previously described. The relevant numerical parameters are described in Table 4. In all the multi- n simulations discussed in this section a Maxwellian control variate has been used, in order to reduce the statistical noise.

The top three panels of Fig. 8 show a snapshot of the poloidal cross section of the electron density (left), the ion gyrocenter density (middle) and the electrostatic potential (right), toward the end of the linear phase. During the linear phase temperature and density profiles do not evolve in time, as it is clearly illustrated by the bottom middle

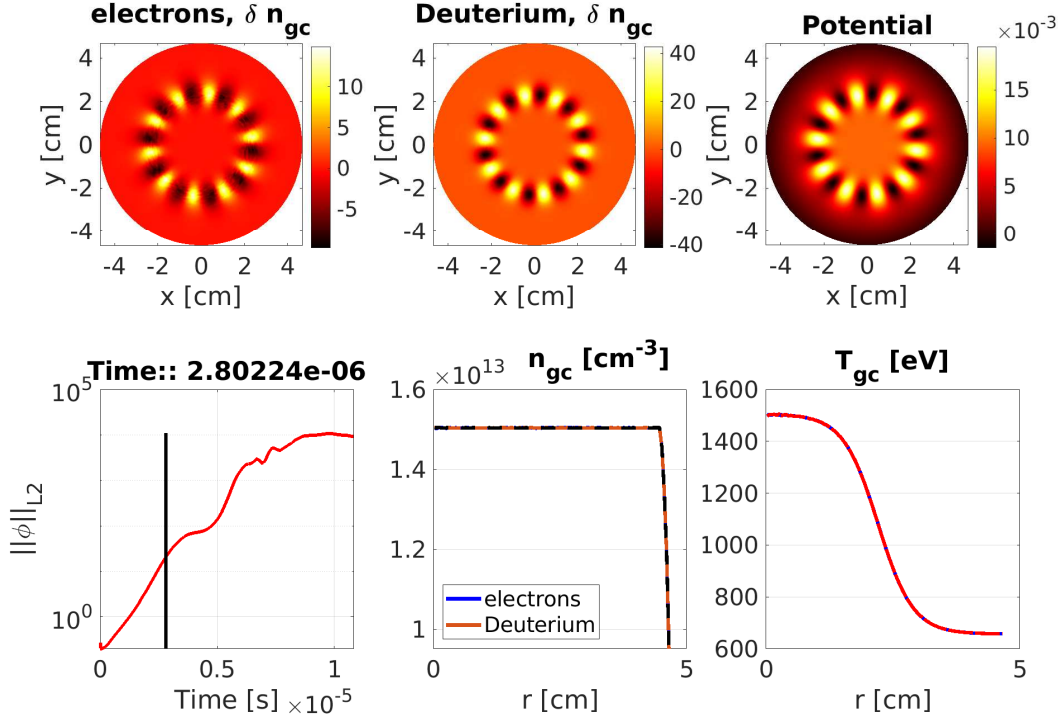


Figure 8. Top line: snapshot of the poloidal cross section of the electron density fluctuation (left), ion gyrocenter density fluctuation (middle) and electrostatic potential (right) at the end of the linear phase. Bottom line: time evolution of the L_2 norm of the electrostatic potential (left) and snapshot of the density (middle) and temperature (left) at the end of the linear phase. The resulting electrostatic potential correctly reflects the properties of the linear elliptic field equation solved by PICLS.

Table 4. PICLS numerical setup for ITG turbulence simulations.

Parameter	Value	Description
nptot el.	128 M	number of electron markers
nptot ions	128 M	number of ion markers
n_r	100	number of splines in r
n_θ	128	number of splines in θ
n_φ	32	number of splines in φ
dt	$2 \cdot 10^{-8}$ s	time step

and right panels of Fig. 8.

The time evolution of the L_2 norm of the electrostatic potential is shown in the left panel of the bottom line. The vertical black line indicates the time at which the snapshot of the other five panels was taken. We can identify three phases characterizing the time evolution of the system. During the first phase, the initial perturbation grows linearly in time, being an unstable Eigenmode of the system. At around time $T = 4 \cdot 10^{-6}$ s a second mode, with higher linear growth rate (and lower k_{\parallel}) becomes the most unstable

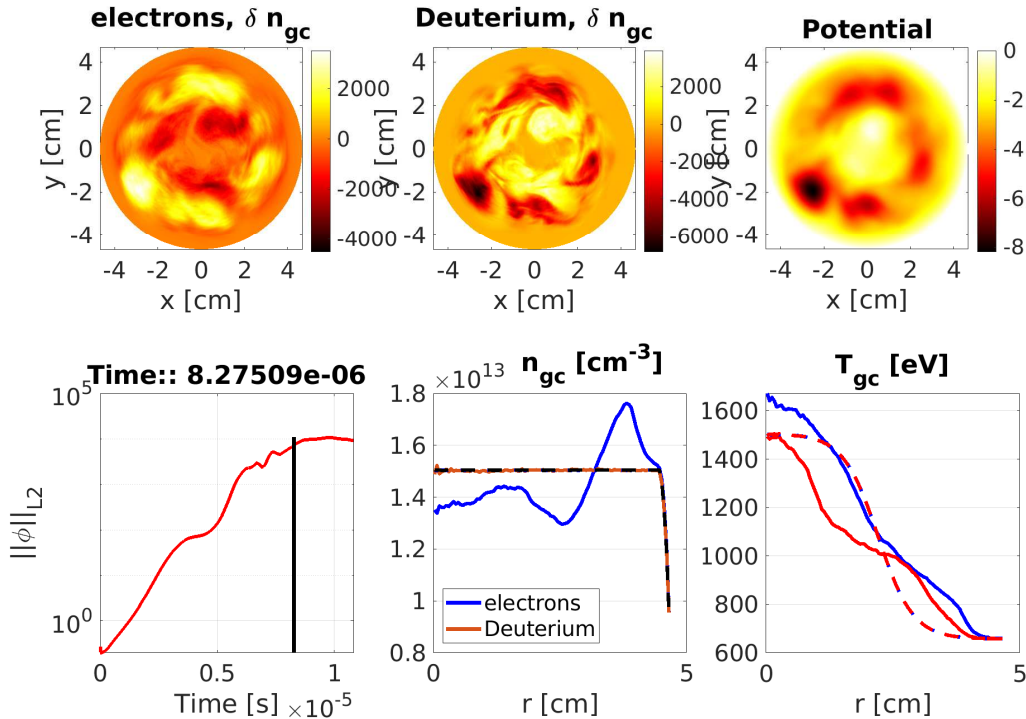


Figure 9. Top line: snapshot of the poloidal cross section of the electron density fluctuation (left), ion gyrocenter density fluctuation (middle) and electrostatic potential (right) during the saturation phase. Bottom line: time evolution of the L_2 norm of the electrostatic potential (left) and snapshot of the density (middle) and temperature (left) during the saturation phase.

mode and dominates the dynamic.

Figure 9 illustrates what happens at later times, when nonlinear terms dominate the dynamics and the turbulence saturates. The electrostatic potential clearly shows the formation of zonal structures, the so-called zonal flows (ZFs). Note that ZFs are not the only possible saturation mechanism in this kind of simulations since no sources are applied to prevent the relaxation of the temperature profiles and the consequently reduced drive. Temperature profile relaxation is indeed visible in both the ion and electron temperatures of Fig. 9. Note that also the boundary conditions can play a significant role in determining the saturation level of such a system.

Nevertheless, it is important to verify that PICLS is able to catch the physics related to ZFs. Therefore, we have repeated the same simulation but keeping only $n = [1 : 5]$ modes in the solver, thus suppressing the zonal component of the potential. Figure 10 compares the ion density fluctuations of the two simulations w/o (left) and with (right) ZFs, during the linear phase (top), the early saturation (middle) and at the end of the simulation (bottom). Being the ZFs linearly stable, they do not play any role during the linear evolution of the system. On the other hand, at saturation, density blobs tend to rotate along the zonal potential structures, while they drift rapidly toward the plasma

edge when the ZF is filtered out. Moreover, Fig. 10 also illustrates the capability of PICLS of dealing with large fluctuations, of the order of the background density.

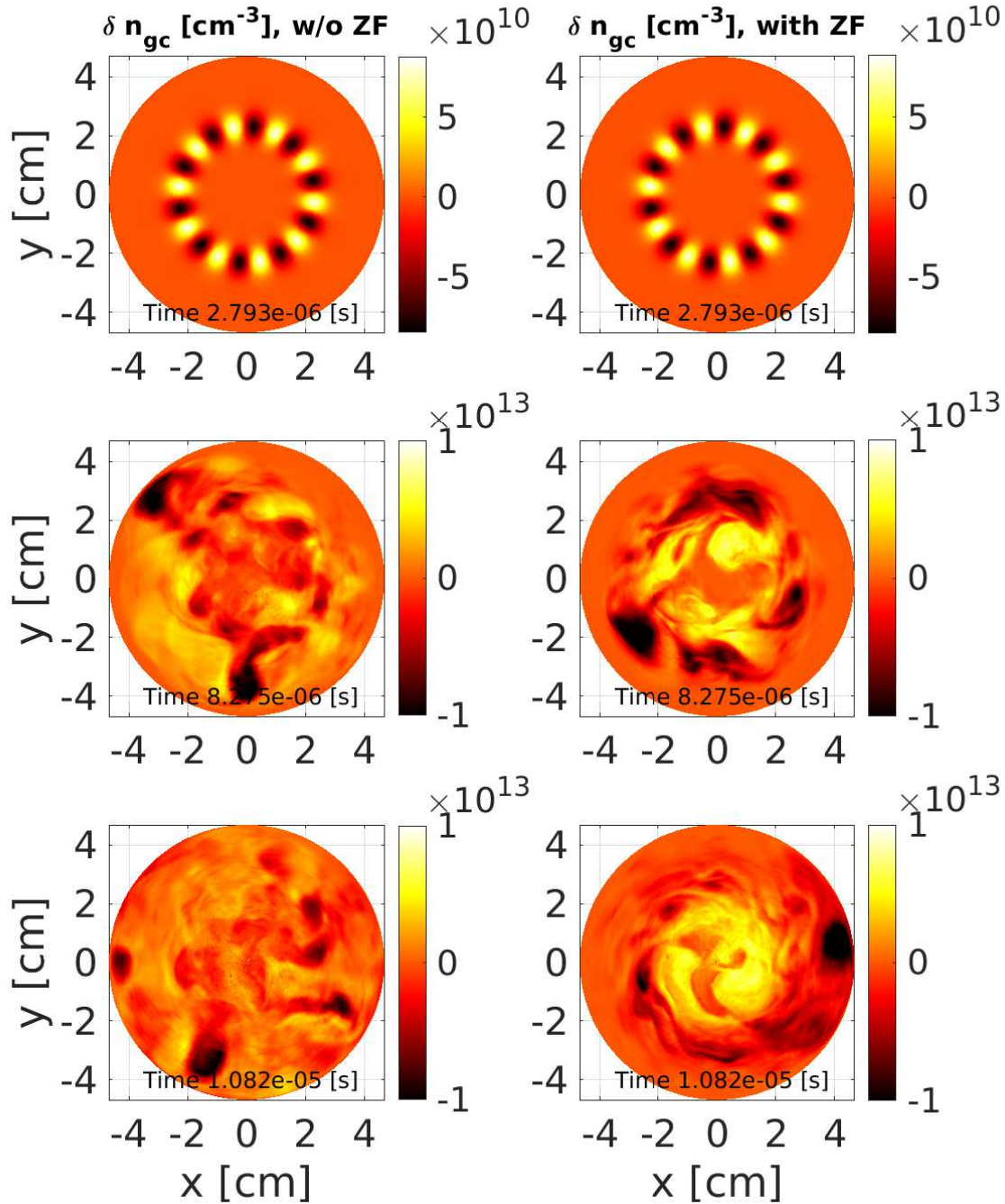


Figure 10. Snapshots of the poloidal cross section of the ion gyrocenter density fluctuations during the linear phase (top), the early saturation phase (middle) and at the last time step (bottom) for two simulations w/o (left) and with (right) Zonal Flows. The Zonal Flow has been suppressed by filtering out the $n = 0$ component in the field solver. During the saturation phase, large density blobs are created, with an amplitude even larger than the initial background density.

3.3. Omega-H mode, comparison with ORB5

The case discussed in this section is inspired by Ref. [63] where a Shear Alfvén Wave (SAW) was simulated using ORB5. This test case was specifically designed to minimize the kinetic corrections to the wave. This was achieved by choosing a Tokamak magnetic equilibrium with very large aspect ratio ($R/a = 100$) and a flat q profile. An initial ion density perturbation was imposed, with a radial Gaussian shape and a poloidal mode number $m = 1$ ($n = 0$). This initial perturbation also excites a damped sound wave, making the interpretation of the results complicated (two damped waves in the system). Therefore, the ion weight distribution was reset to the Maxwellian distribution after the first call to the solver, in order to suppress the sound wave related to the initial ion pressure perturbation.

As mentioned before, PICLS is an electrostatic code, although an electromagnetic version is under development. Therefore, a direct comparison with the published ORB5 results is not possible. Nevertheless, the SAW has an electrostatic counterpart, the so-called Omega-H mode. The Omega-H mode [24] is an Eigenmode of the electrostatic system which does not have a correspondent in nature. The dispersion relation of the Omega-H mode is obtained by taking the $\beta \rightarrow 0$ limit while keeping the sound velocity c_s finite in the kinetic dispersion relation of a SAW. The simplest SAW kinetic dispersion relation, see e.g. [64] is

$$\omega_{SAW,KIN}^2 = v_A^2 \frac{1 + k_{\perp}^2 \rho_s^2}{1 + k_{\perp}^2 d_e^2} k_{\parallel} = 2c_s^2 \frac{1 + k_{\perp}^2 \rho_s^2}{\beta_e + k_{\perp}^2 \rho_s^2} k_{\parallel}. \quad (24)$$

The Omega-H dispersion relation is obtained by setting $\beta_e = 0$ but keeping c_s finite, leading to

$$\omega_H^2 = 2c_s^2 \frac{1 + k_{\perp}^2 \rho_s^2}{k_{\perp}^2 \rho_s^2} k_{\parallel}, \quad (25)$$

with

$$c_s^2 = \frac{T_e}{m_1}, v_A^2 = \frac{B_0^2}{\mu_0 n m_i}, \beta_e = \frac{2\mu_0 p_e}{B_0^2} = 2 \frac{c_s^2}{v_a^2}, \quad (26)$$

$$d_e^2 = \frac{m_i}{2\mu_0 n q_i}, \rho_s = \frac{c_s}{\Omega_{ci}}, \Omega_{ci} = \frac{q_i B_0}{m}, k_{\parallel} = \frac{1}{qR}. \quad (27)$$

The code ORB5 has been rerun using the same input of Ref. [63], with the exception of the choice of the electrostatic model for the field equations. Fig. 11 shows the time evolution of the L_2 norm (in arbitrary units) for the two codes, showing an excellent agreement on the frequency of the Omega-H mode. Note that the background temperature has been set to a very low value (100 eV) in order to minimize the Landau damping. Fig. 12 shows the dependency of the frequency of the Omega-H mode on the safety factor q in PICLS simulations. The expected $1/q$ dependence in k_{\parallel} of the dispersion relation is retrieved.

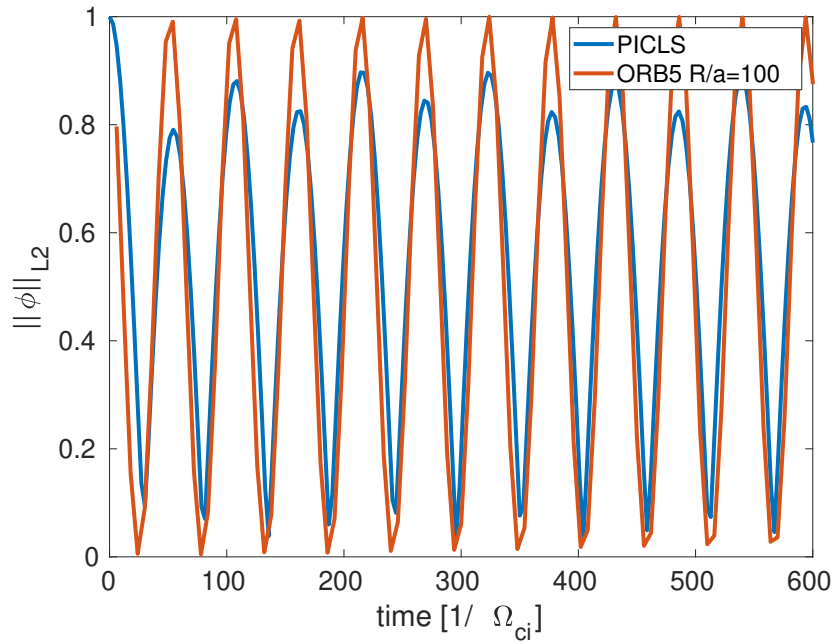


Figure 11. Time evolution of the L_2 norm of the electrostatic potential for ORB5 and PICLS, using the setup described in Table 5.

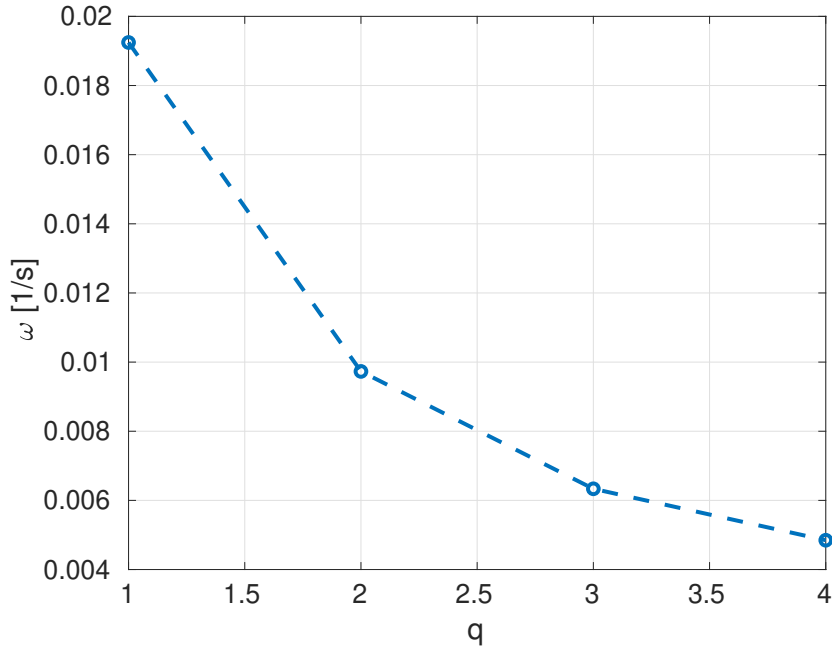


Figure 12. Frequency of the Omega-H mode as a function of the (constant) safety factor using PICLS with the setup described in Table 5.

4. Conclusions

The PICLS code has been extended to a 3D spatial domain. Since going from 1D to 3D included significant changes in the models and algorithms applied, we have presented

Table 5. PICLS geometric setup and initial perturbation for the simulations of Figs. 11 and 12.

Parameter	Value	Description
a	1.67 [cm]	minor radius
R	167 [cm]	major radius
n_0	10^{15} [cm $^{-3}$]	density (flat)
B_0	2.4[T]	magnetic field on axis
$T_{e0} = T_{i0}$	100 [eV]	temperature(flat)
m_{init}	1	initial poloidal mode
n_{init}	0	initial toroidal mode
q	2 (flat)	safety factor ⁴
m_e	$1 m_{elec}$	electron mass
m_i	$3972 m_{elec}$	ion mass

here a number of verification tests for closed-field-line geometry. Key features of the 3D code are the 3D importance sampling particle loading, the gyroaverage algorithm and the Fourier enhanced field solver [57]. Concerning the field solver, we have applied the Method of Manufactured Solutions to a physically relevant 3D case. Finally, we have verified the code by comparing with the two well established GENE-X and ORB5 codes, for two different problems. Both verification tests were passed. We have also shown that PICLS can cope with large density fluctuations, comparable in size or even large than the background, which is a crucial requirement for future SOL applications.

Acknowledgments

The authors wish to thank Roman Hatzky and Emanuele Poli for fruitful discussions. This work has been carried out within the framework of the EUROfusion Consortium, partially funded by the European Union via the Euratom Research and Training Programme (Grant Agreement No 101052200 — EUROfusion). The Swiss contribution to this work has been funded by the Swiss State Secretariat for Education, Research and Innovation (SERI). Views and opinions expressed are however those of the author(s) only and do not necessarily reflect those of the European Union, the European Commission or SERI. Neither the European Union nor the European Commission nor SERI can be held responsible for them. Part of the simulations discussed in this work were performed on the MARCONI FUSION HPC system at CINECA.

- [1] S. J. Zweben, J. A. Boedo, O. Grulke, C. Hidalgo, B. LaBombard, R. J. Maqueda, P. Scarin, and J. L. Terry. Edge turbulence measurements in toroidal fusion devices. *PLASMA PHYSICS AND CONTROLLED FUSION*, 49(7):S1–S23, 07 2007. IEA Large Tokamak IA Workshop on Edge Transport in Fusion Plasmas, Cracow, POLAND, SEP 11-13, 2006.
- [2] P.C. Stangeby. *The plasma boundary of magnetic fusion devices*. CRC Press, 2000.
- [3] P. Ricci. Simulation of the scrape-off layer region of tokamak devices. *Journal of Plasma Physics*, 81(2):435810202, 2015.

- [4] A. Masetto, F. D. Halpern, S. Jolliet, J. Loizu, and P. Ricci. Turbulent regimes in the tokamak scrape-off layer. *Physics of Plasmas*, 20(9):092308, 2013.
- [5] R. H. Cohen, N. Mattor, and X. Xu. Scrape-off layer turbulence theory. *Contributions to Plasma Physics*, 34(2-3):232–246, 1994.
- [6] L. Isoardi, G. Chiavassa, G. Ciraolo, P. Haldenwang, E. Serre, Ph. Ghendrih, Y. Sarazin, F. Schwander, and P. Tamain. Penalization modeling of a limiter in the tokamak edge plasma. *Journal of Computational Physics*, 229(6):2220–2235, 2010.
- [7] David Tskhakaya, R.A. Pitts, Wojciech Fundamenski, T Eich, S Kuhn, and JET EFDA Contributors. Kinetic simulations of the parallel transport in the jet scrape-off layer. *Journal of Nuclear Materials*, 390-391, 06 2009.
- [8] Giovanni Manfredi, Sever Adrian Hirstoaga, Stéphane Devaux, Eva Havlickova, and David Tskhakaya. Parallel transport in a tokamak scrape-off layer. *38th EPS Conference on Plasma Physics 2011, EPS 2011 - Europhysics Conference Abstracts*, 35, 06 2011.
- [9] R Schneider, D Reiter, HP Zehrfeld, B Braams, Martine Baelmans, J Geiger, H Kastelewicz, J Neuhauser, and R Wunderlich. B2-eirene simulation of asdex and asdex-upgrade scrape-off layer plasmas. *Journal of nuclear materials*, 196:810–815, 1992.
- [10] R Schneider, X Bonnin, K Borrass, DP Coster, H Kastelewicz, D Reiter, VA Rozhansky, and BJ Braams. Plasma edge physics with b2-eirene. *Contributions to Plasma Physics*, 46(1-2):3–191, 2006.
- [11] V Rozhansky, E Kaveeva, P Molchanov, I Veselova, S Voskoboynikov, D Coster, G Counsell, A Kirk, S Lisgo, MAST Team, et al. New b2solps5. 2 transport code for h-mode regimes in tokamaks. *Nuclear Fusion*, 49(2):025007, 2009.
- [12] Andreas Stegmeir, David Coster, Alexander Ross, Omar Maj, Karl Lackner, and Emanuele Poli. Grillix: a 3d turbulence code based on the flux-coordinate independent approach. *Plasma Physics and Controlled Fusion*, 60(3):035005, 2018.
- [13] W Zholobenko, A Stegmeir, T Body, A Ross, P Manz, O Maj, D Coster, F Jenko, M Francisquez, B Zhu, et al. Thermal dynamics in the flux-coordinate independent turbulence code grillix. *Contributions to Plasma Physics*, 60(5-6):e201900131, 2020.
- [14] Bruce D Scott. Computation of electromagnetic turbulence and anomalous transport mechanisms in tokamak plasmas. *Plasma physics and controlled fusion*, 45(12A):A385, 2003.
- [15] T Takizuka. Kinetic effects in edge plasma: kinetic modeling for edge plasma and detached divertor. *Plasma Physics and Controlled Fusion*, 59(3):034008, feb 2017.
- [16] Natalia Tronko, Alberto Bottino, and Eric Sonnendrücker. Second order gyrokinetic theory for particle-in-cell codes. *Physics of Plasmas*, 23(8):082505, 2016.
- [17] H. Sugama. Gyrokinetic field theory. *Physics of Plasmas*, 7:466, 2000.
- [18] A.J. Brizard. Variational principle for nonlinear gyrokinetic Vlasov-Maxwell equations. *Physics of Plasmas*, 7(12):4816–4822, 2000.
- [19] Choong Seock Chang, S Ku, Alberto Loarte, Vassili Parail, Florian Koechl, Michele Romanelli, Rajesh Maingi, J-W Ahn, T Gray, J Hughes, et al. Gyrokinetic projection of the divertor heat-flux width from present tokamaks to iter. *Nuclear Fusion*, 57(11):116023, 2017.
- [20] J. Dominski, C.S. Chang, R. Hager, S. Ku, E.S. Yoon, and V. Parail. Neoclassical transport of tungsten ion bundles in total-f neoclassical gyrokinetic simulations of a whole-volume JET-like plasma. *Physics of Plasmas*, 31(3):032303, 03 2024.
- [21] J. Dominski, C.S. Chang, R. Hager, P. Helander, S. Ku, and E.S. Yoon. Study of up–down poloidal density asymmetry of high- Z impurities with the new impurity version of XGCa. *Journal of Plasma Physics*, 85(5):905850510, 2019.
- [22] R. Hager, C.S. Chang, N.M. Ferraro, and R. Nazikian. Gyrokinetic study of collisional resonant magnetic perturbation (rmp)-driven plasma density and heat transport in tokamak edge plasma using a magnetohydrodynamic screened rmp field. *Nuclear Fusion*, 59(12):126009, sep 2019.
- [23] A. Bottino and E. Sonnendrücker. Monte Carlo particle-in-cell methods for the simulation of the Vlasov–Maxwell gyrokinetic equations. *Journal of Plasma Physics*, 81(5), 2015.

- [24] WW Lee. Gyrokinetic approach in particle simulation. *The Physics of Fluids*, 26(2):556–562, 1983.
- [25] S. Ku, R. Hager, C.S. Chang, J.M. Kwon, and S.E. Parker. A new hybrid-lagrangian numerical scheme for gyrokinetic simulation of tokamak edge plasma. *Journal of Computational Physics*, 315:467–475, 2016.
- [26] Frank Jenko and W Dorland. Nonlinear electromagnetic gyrokinetic simulations of tokamak plasmas. *Plasma Physics and Controlled Fusion*, 43(12A):A141, 2001.
- [27] A.H. Hakim, N.R. Mandell, T.N. Bernard, M. Francisquez, G.W. Hammett, and E.L. Shi. Continuum electromagnetic gyrokinetic simulations of turbulence in the tokamak scrape-off layer and laboratory devices. *Physics of Plasmas*, 27(4), 2020. Cited by: 24; All Open Access, Bronze Open Access.
- [28] John A Krommes. The gyrokinetic description of microturbulence in magnetized plasmas. *Annual Review of Fluid Mechanics*, 44:175–201, 2012.
- [29] David Tskhakaya, K Matyash, R Schneider, and F Taccogna. The particle-in-cell method. *Contributions to Plasma Physics*, 47(8-9):563–594, 2007.
- [30] R.W. Hockney and J.W. Eastwood. *Computer simulation using particles*. CRC Press, 1988.
- [31] C.K. Birdsall and A.B. Langdon. *Plasma physics via computer simulation*. CRC Press, 2004.
- [32] X. Garbet, Y. Idomura, L. Villard, and T.H. Watanabe. Gyrokinetic simulations of turbulent transport. *Nuclear Fusion*, 50(4):043002, 2010.
- [33] John A Krommes. Nonequilibrium gyrokinetic fluctuation theory and sampling noise in gyrokinetic particle-in-cell simulations. *Physics of Plasmas*, 14(9):090501, 2007.
- [34] A Bottino, AG Peeters, R Hatzky, S Jolliet, BF McMillan, TM Tran, and L Villard. Nonlinear low noise particle-in-cell simulations of electron temperature gradient driven turbulence. *Physics of plasmas*, 14(1):010701, 2007.
- [35] Roman Hatzky, Axel Könies, and Alexey Mishchenko. Electromagnetic gyrokinetic pic simulation with an adjustable control variates method. *Journal of Computational Physics*, 225(1):568–590, 2007.
- [36] Alexey Mishchenko, Roman Hatzky, and Axel Könies. Conventional δf -particle simulations of electromagnetic perturbations with finite elements. *Physics of plasmas*, 11(12):5480–5486, 2004.
- [37] R Kleiber, R Hatzky, A Könies, A Mishchenko, and E Sonnendrücker. An explicit large time step particle-in-cell scheme for nonlinear gyrokinetic simulations in the electromagnetic regime. *Physics of Plasmas*, 23(3):032501, 2016.
- [38] Alexey Mishchenko, Alberto Bottino, Roman Hatzky, Eric Sonnendrücker, Ralf Kleiber, and Axel Könies. Mitigation of the cancellation problem in the gyrokinetic particle-in-cell simulations of global electromagnetic modes. *Physics of Plasmas*, 24(8):081206, 2017.
- [39] Yasuhiro Idomura. Full-f gyrokinetic simulation over a confinement time. *Physics of Plasmas*, 21(2):022517, 2014.
- [40] XQ Xu, Z Xiong, MR Dorr, JA Hittinger, K Bodi, J Candy, BI Cohen, RH Cohen, P Colella, GD Kerbel, et al. Edge gyrokinetic theory and continuum simulations. *Nuclear fusion*, 47(8):809, 2007.
- [41] Bruce D Scott, A Kendl, and T Ribeiro. Nonlinear dynamics in the tokamak edge. *Contributions to Plasma Physics*, 50(3-5):228–241, 2010.
- [42] Wonjae Lee, MA Dorf, MR Dorr, RH Cohen, TD Rognlien, JAF Hittinger, MV Umansky, and SI Krasheninnikov. Verification of 5d continuum gyrokinetic code cogent: Studies of kinetic drift wave instability. *Contributions to Plasma Physics*, 58(6-8):445–450, 2018.
- [43] AH Hakim, GW Hammett, and EL Shi. On discontinuous galerkin discretizations of second-order derivatives. *arXiv preprint arXiv:1405.5907*, 2014.
- [44] EL Shi, GW Hammett, T Stoltzfus-Dueck, and A Hakim. Gyrokinetic continuum simulation of turbulence in a straight open-field-line plasma. *Journal of Plasma Physics*, 83(3):905830304, 2017.
- [45] Eric L Shi, Gregory W Hammett, Timothy Stoltzfus-Dueck, and Ammar Hakim. Full-f gyrokinetic

- simulation of turbulence in a helical open-field-line plasma. *Physics of Plasmas*, 26(1):012307, 2018.
- [46] Dominik Michels, Andreas Stegmeir, Philipp Ulbl, Denis Jarema, and Frank Jenko. Gene-x: A full-f gyrokinetic turbulence code based on the flux-coordinate independent approach. *Computer Physics Communications*, 264:107986, 2021.
- [47] M. Boesl, A. Bergmann, A. Bottino, D. Coster, E. Lanti, N. Ohana, and F. Jenko. Gyrokinetic full-f particle-in-cell simulations on open field lines with PICLS. *Physics of Plasmas*, 26(12):122302, 2019.
- [48] M. Boesl, A. Bergmann, A. Bottino, S. Brunner, D. Coster, and F. Jenko. Collisional gyrokinetic full-f particle-in-cell simulations on open field lines with PICLS. *Contributions to Plasma Physics*, page e201900117, 12 2019.
- [49] A Loarte, B Lipschultz, AS Kukushkin, GF Matthews, PC Stangeby, N Asakura, GF Counsell, G Federici, A Kallenbach, K Krieger, et al. Power and particle control. *Nuclear Fusion*, 47(6):S203, 2007.
- [50] S.E. Parker, R.J. Procassini, Birdsall C.K., and Cohen B.I. A suitable boundary condition for bounded plasma simulation without sheath resolution. *Journal of Computational Physics*, 104(1):41–49, 1993.
- [51] N. Tronko and C. Chandre. Second-order nonlinear gyrokinetic theory: from the particle to the gyrocentre. *Journal of Plasma Physics*, 84(3), 2018.
- [52] D.H.E. Dubin, J.A. Krommes, C. Oberman, and W.W. Lee. Nonlinear gyrokinetic equations. *Physics of Fluids*, 26(12):3524–3535, 1983.
- [53] E. Lanti, N. Ohana, N. Tronko, T. Hayward-Schneider, A. Bottino, B. F. McMillan, A. Mishchenko, A. Scheinberg, A. Biancalani, P. Angelino, S. Brunner, J. Dominski, P. Donnel, C. Gheller, R. Hatzky, A. Jocksch, S. Jolliet, Z. X. Lu, J. P. Martin Collar, I Novikau, E. Sonnendruecker, T. Vernay, and L. Villard. Orb5: A global electromagnetic gyrokinetic code using the PIC approach in toroidal geometry. *COMPUTER PHYSICS COMMUNICATIONS*, 251, JUN 2020.
- [54] R. Hatzky, R. Kleiber, A. Könies, A. Mishchenko, M. Borchardt, A. Bottino, and E. Sonnendrücker. Reduction of the statistical error in electromagnetic gyrokinetic particle-in-cell simulations. *Journal of Plasma Physics*, 85(1):905850112, 2019.
- [55] J. Dominski, S. Ku, and C.S. Chang. Gyroaveraging operations using adaptive matrix operators. *Physics of Plasmas*, 25(5):052304, 05 2018.
- [56] A. Bottino, M.V. Falessi, T. Hayward-Schneider, A. Biancalani, S. Briguglio, R. Hatzky, Ph. Lauber, A. Mishchenko, E. Poli, B. Rettino, F. Vannini, X. Wang, and F. Zonca. Time evolution and finite element representation of phase space zonal structures in orb5. *Journal of Physics: Conference Series*, 2397(1):012019, dec 2022.
- [57] A. Stier, A. Bottino, M. Boesl, M. Campos Pinto, A. Bergmann, M. Murugappan, S. Brunner, L. Villard, and F. Jenko. Verification of the fourtier-enhanced 3d finite element poisson solver of the gyrokinetic full-f code picls. *Computer Physics Communications*, 229:109155, 2024.
- [58] E. Anderson, Z. Bai, C. Bischof, S. Blackford, J. Demmel, J. Dongarra, J. Du Croz, A. Greenbaum, S. Hammarling, A. McKenney, and D. Sorensen. *LAPACK Users' Guide*. Society for Industrial and Applied Mathematics, Philadelphia, PA, third edition, 1999.
- [59] William L Oberkampf and Christopher J Roy. *Verification and validation in scientific computing*. Cambridge University Press, 2010.
- [60] S.E. Parker, R.J. Procassini, C.K. Birdsall, and B.I. Cohen. A suitable boundary condition for bounded plasma simulation without sheath resolution. *Journal of Computational Physics*, 104(1):41–49, 1993.
- [61] Satoshi Togo, Tomonori Takizuka, Makoto Nakamura, Kazuo Hoshino, Kenzo Ibano, Tee Long Lang, and Yuichi Ogawa. Self-consistent treatment of the sheath boundary conditions by introducing anisotropic ion temperatures and virtual divertor model. *Journal of Computational Physics*, 310:109–126, 2016.
- [62] R. Hatzky. Domain cloning for a particle-in-cell (pic) code on a cluster of symmetric-multiprocessor

- (smp) computers. *Parallel Computing*, 32(4):325–330, 2006.
- [63] A. Biancalani, A. Bottino, S. Briguglio, A. Könies, Ph. Lauber, A. Mishchenko, E. Poli, B. D. Scott, and F. Zonca. Linear gyrokinetic particle-in-cell simulations of Alfvén instabilities in tokamaks. *Physics of Plasmas*, 23(1):012108, 01 2016.
- [64] R.L. Lysak. Kinetic alfvén waves and auroral particle acceleration: a review. *Rev. Mod. Plasma Phys.*, page 6, 7 2023.